Science Advances
AAAS

advances.sciencemag.org/cgi/content/full/6/39/eabb1601/DC1

Supplementary Materials for

The role of ultrafast magnon generation in the magnetization dynamics of rare-earth metals

B. Frietsch, A. Donges, R. Carley, M. Teichmann, J. Bowlan, K. Döbrich, K. Carva, D. Legut, P. M. Oppeneer, U. Nowak, M. Weinelt*

*Corresponding author. Email: weinelt@physik.fu-berlin.de

Published 23 September 2020, *Sci. Adv.* **6**, eabb1601 (2020)
DOI: 10.1126/sciadv.abb1601

This PDF file includes:

SUPPLEMENTARY MATERIAL

I. EVALUATION OF THE ARPES DATA

A. Time-resolved ARPES spectra

In the time-resolved ARPES experiment the sample was pumped by 1.60 eV NIR pulses with pulse duration of 100 and 300 fs for Tb and Gd, respectively. Due to the lower work function of Gd (3.7 eV) as compared to Tb (5.2 eV) pump pulses for Gd had to be stretched to avoid multiphoton photoemission and pump-induced space charge [33]. The absorbed pump fluence was 2.5 mJ/cm^2 in Tb and 3.5 mJ/cm^2 in Gd. Higher pump fluences for Tb resulted in a multidomain state, *i.e.* the magnetization did not fully recover without external field.

Figures S1 shows photoemission data for Tb recorded for varying pump-probe delay at a photon energy of $\hbar\omega = 40.0$ eV, corresponding to the 25th harmonics of the laser fundamental. Figure S1a depicts a grayscale plot of the photoemission map before optical excitation at -1 ps delay. The energy distribution curves (EDCs) in Fig. S1b were extracted along the ΓM direction at an emission angle of 0° with an acceptance angle of ±2.5° (see the rectangle in Fig. S1a). The corresponding lineouts show spectra for both magnetization directions (red and blue). The occupied majority component of the Tamm-like surface state close to the Fermi level E_F indicates the high quality of the Tb film preparation. The peak at ~ 5.8 eV binding energy stems from a small oxygen contamination adsorbed at the film surface. At a photon energy of $\hbar\omega = 40.0$ eV and normal emission the energy distribution curves are dominated by the 4f high spin multiplet component $^8S_{7/2}$ and we can follow the dynamics of the 4f magnetic linear dichroism (MLD) already in the photoemission raw data. Obviously, at a pump-probe delay of ~ 1.0 ps the MLD, *i.e.* the difference between red and blue spectra (see green EDC in Fig. S1c), is the smallest and recovers at around 100 ps. This ultrafast decay of the 4f MLD signal matches the dynamics of the 5d exchange splitting. To measure the 5d valence band exchange splitting Δ_{ex}, we tuned the photon energy to the 23rd harmonics at 36.8 eV (see Fig. S2). At this energy photoemission follows the Δ_2-like component of the valence bands in the 4$^{\text{th}}$ Brillouin zone. As seen from Figs. S2a and b at a photon energy of 36.8 eV and for off-normal emission (rectangles in Figs. S2a

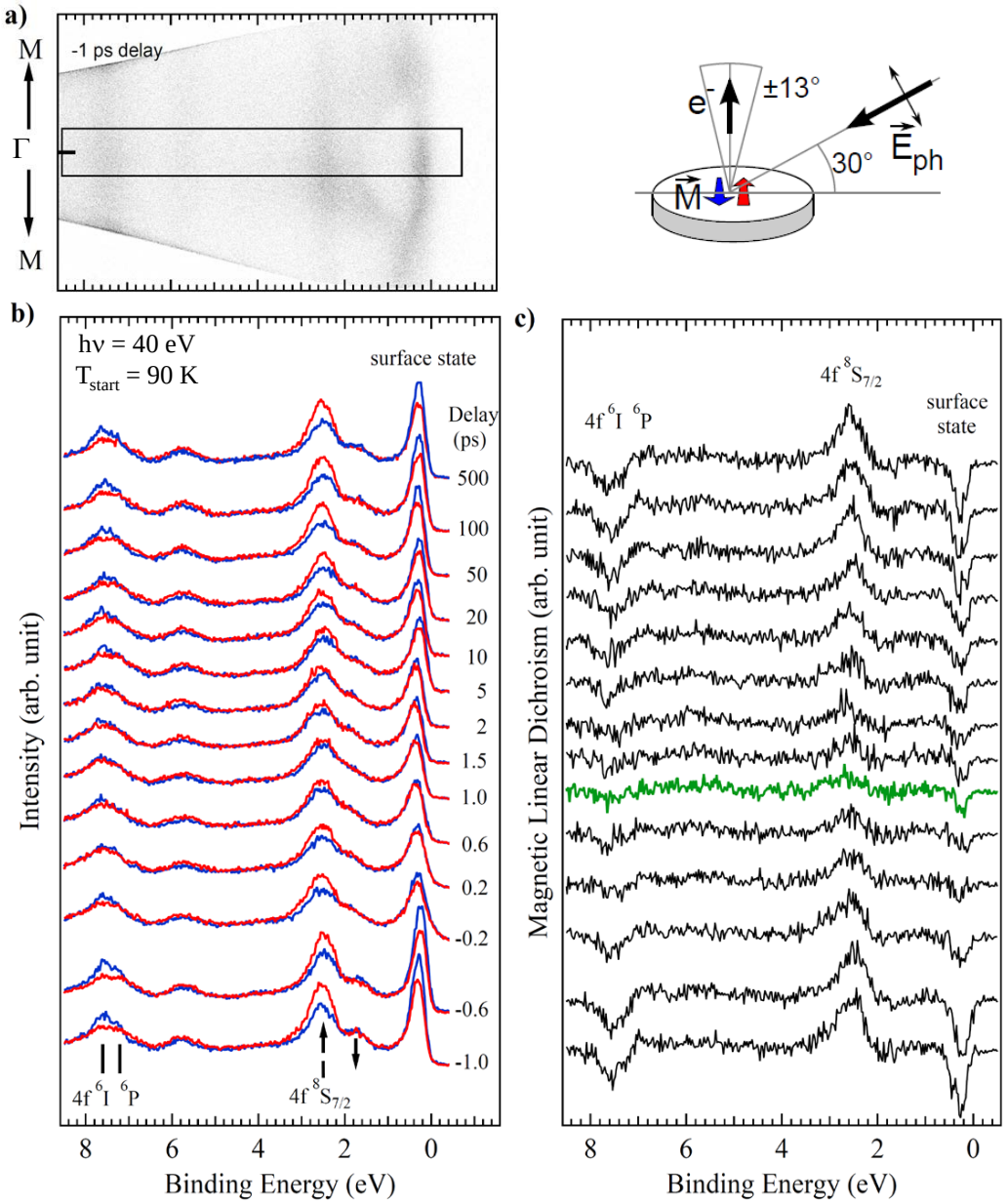

FIG. S1. Tb ARPES data recorded as a function of pump-probe delay for opposite in-plane magnetization directions ±M with p-polarized light at a photon energy of 40.0 eV. a) 2D photoemission map before laser excitation. b) Energy distribution curves for both magnetization directions were extracted at an emission angle of ±2.5° indicated by the square in a). At a photon energy of 40.0 eV (25th harmonics) the 4f high-spin multiplet component at 2.5 eV binding energy dominates over the valence-band photoemission. Indicated are the exchange split (5d) majority (↑) and minority (↓) spin valence bands as well as the 4f components $^8S_{7/2}$, ^6P and ^6I. c) Difference spectra I(+M) - I(-M) illustrating the transient magnetic linear dichroism of the surface state and the 4f multiplets. All components show a minimum at a delay of ~ 1 ps.

and b) the minority and majority spin components (↓ and ↑) dominate over the 4f high spin component at 2.5 eV. Arrows in Fig. S2c highlight the transient binding energy of the minority and majority spin valence bands. Before excitation at -1 ps delay binding energies are 0.95 and 1.7 eV, respectively. At 1 ps delay the two spin bands merge resulting in a significant reduction the exchange splitting to halve its initial value. We evaluated the exchange splitting in detail by a fit, including the surface state, the majority and minority spin components of the valence band, the 4f high spin multiplet, and two backgrounds accounting for elastic and inelastic electron scattering. Paralleling the 4f dynamics, the exchange splitting reaches its minimum within the first $\sim$ 1 ps after laser excitation and recovers at around 100 ps pump-probe delay (see Fig. S4). For a complete set of EDCs we refer to Teichmann *et al.* [21].

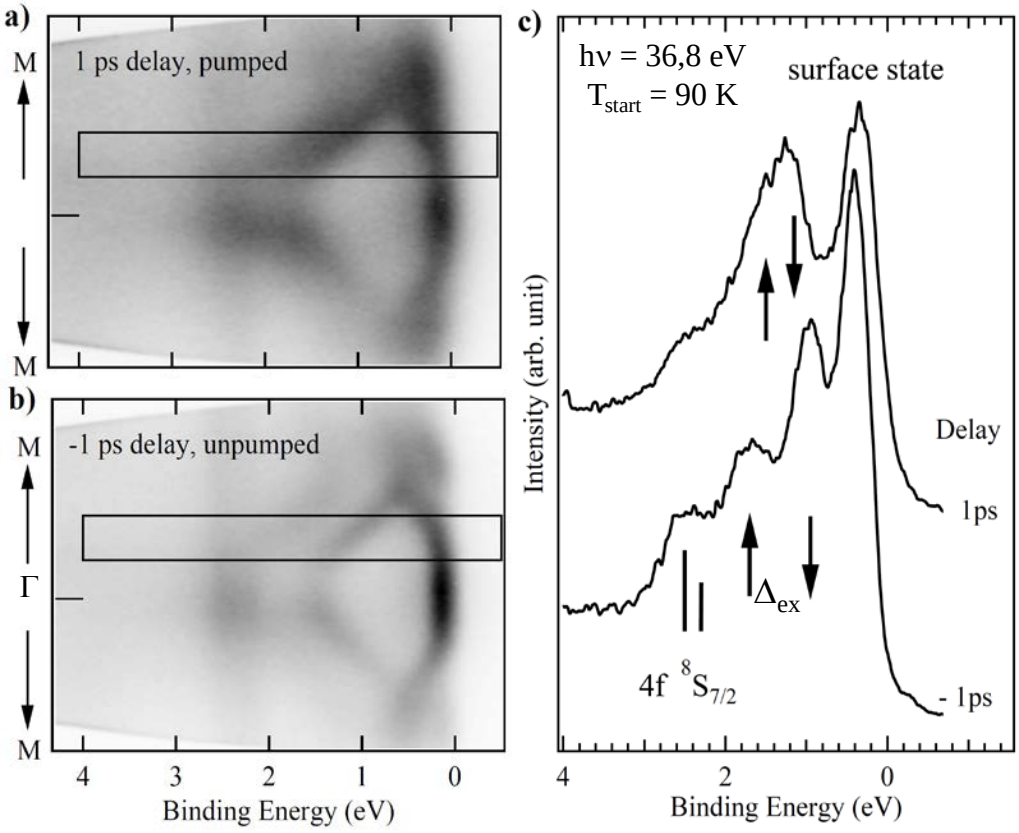

FIG. S2. Tb ARPES data recorded at a photon energy of 36.8 eV. Data for -1 and +1 ps delay have been recorded 1 ps before and after laser excitation, respectively. At 36.8 eV photon energy the photoemission intensity of the valence band dominates over the 4f contributions. Arrows ↓ and ↑ mark the position of the the minority and majority spin components of the valence band.

B. Evaluation of the 4f magnetic linear dichroism

The magnetic linear dichroism (MLD) in the photoemission signal is obtained by integrating the background-subtracted absolute value of the normalized difference of the blue and red spectra in Fig. S1 in the energy range of the 4f multiplets. Thereby we averaged over a detection range of $\pm 13°$ in steps of $1°$. For Tb the pronounced contrast at the high spin final state $^8S_{7/2}$ is particularly suitable for evaluation. However, the common normalization (*i.e.* MLD $\sim |\int I_1 - I_2| / |\int I_1 + I_2|$, where I_1 and I_2 denote recorded intensities for opposite magnetization directions) does not work since the $^8S_{7/2}$ multiplet component overlaps with the 5d majority spin band (see Figs. S1). The latter shifts with pump-probe delay leading to a seemingly slower response of the MLD signal. The low spin multiplet components at 7.5 eV binding energy do not have this problem. Comparing here normalized with non-normalized MLD signal we find no significant difference. We therefore only normalized individual spectra to the probe intensity, *i.e.* we divide each spectrum by its background intensity. Since

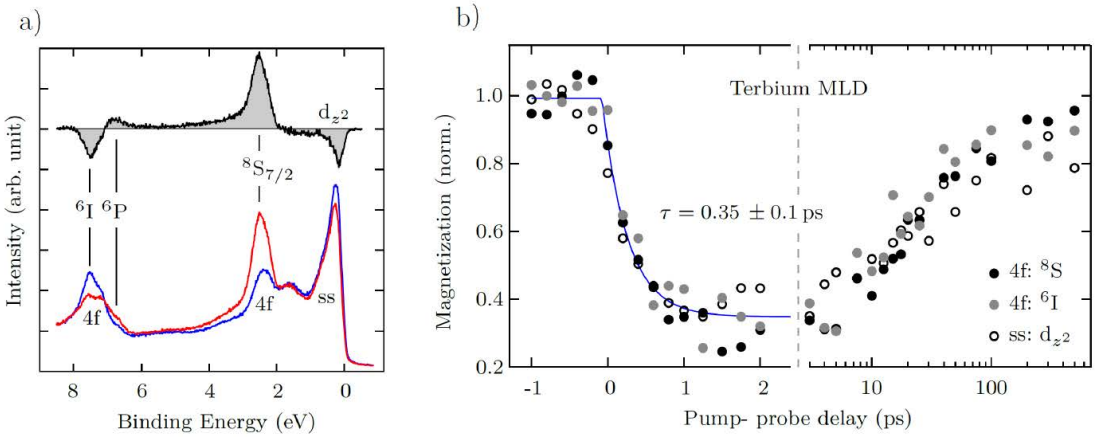

FIG. S3. Magnetic linear dichroism of the Tb low and high spin 4f components and the d_{z^2} surface state recorded at a photon energy of $\hbar\omega = 40.0$ eV (25th harmonic). a) Energy distribution curves at negative pump-probe delay for both magnetization directions (red and blue). The difference spectrum (shaded gray) is used to follow the magnetization of the different lines. b) MLD as a function of pump-probe delay for an absorbed pump fluence of 2.5 mJ/cm^2. The pump-probe delay on the abscissa is bisected and the scale switches from linear to logarithmic. High (•) and low (•) spin final state MLD contributions of the Tb 4f multiplet together with the dichroism from the d_{z^2} surface state (○). The blue line is a single exponential fit to all data points.

the various multiplet components are well separated in the photoelectron spectrum, we can compare the high- and low-spin dynamics of the $^8S_{7/2}$ and ^6I components as well as the small dichroic signal from the $5d_{z^2}$ surface state. As illustrated in Figs. S3 the dynamics of all components is comparable within error bars. All components exhibit the same ultrafast timescale of about 0.35 ± 0.1 ps and the same level of demagnetization.

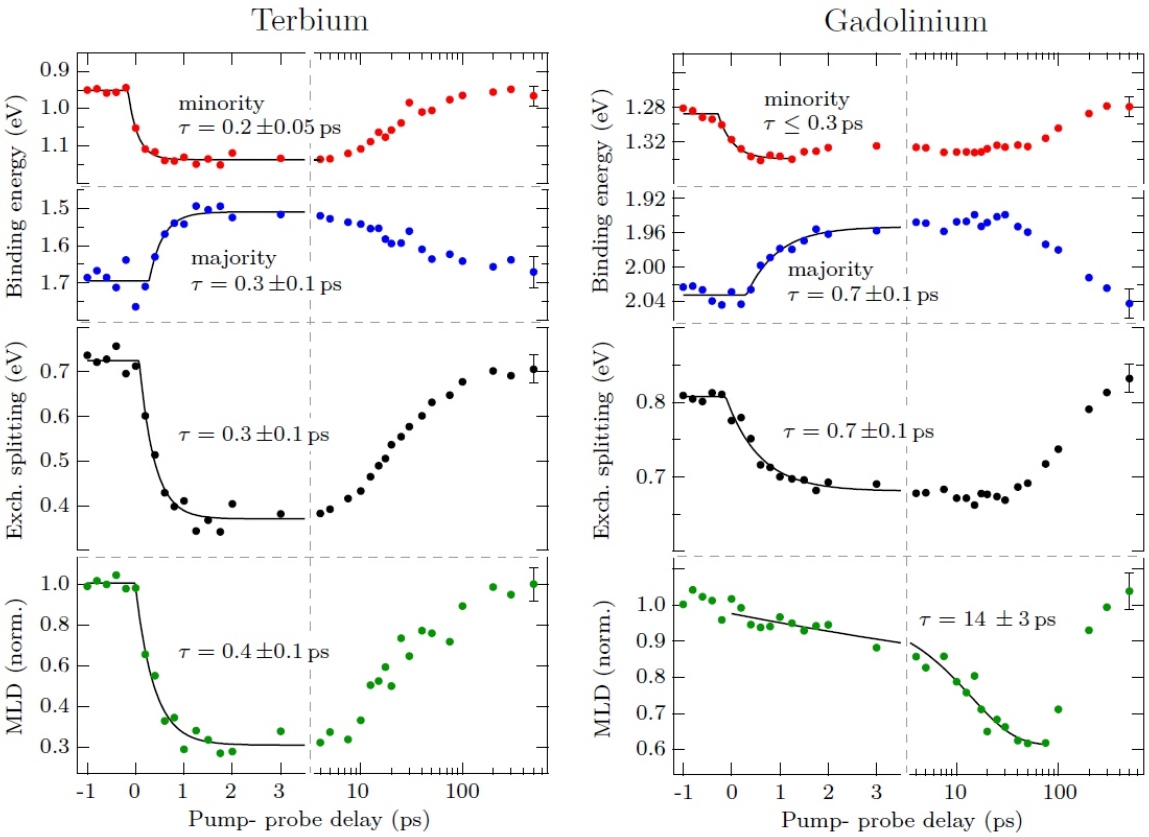

FIG. S4. Magnetization dynamics of itinerant and localized electrons in Gd (left) and Tb (right). The upper panels show the response of the minority (red) and majority (blue) 5d spin bands upon laser excitation. Their dynamics result in a reduction of the exchange splitting (black) with a time constant of 0.3 ps in Tb and 0.7 ps in Gd. In Tb the polarization of the 4f state (green, normalized) follows closely the exchange splitting, while for Gd it stays relatively unperturbed and diminishes with a much slower time constant of 14 ps. Both the exchange splitting and the MLD signals were fitted with a single exponential function to obtain the given time constants. The initial sample temperature is 90 K. The sample is pumped by 100 fs (300 fs for Gd), 1.6 eV photon pulses with an absorbed fluence of 2.5 mJ/cm^2 in Tb and 2.5 mJ/cm^2 in Gd. Error bars on the last data points show two standard deviations.

C. Ultrafast demagnetization dynamics

Figure S4 compares the magnetization dynamics in Tb and Gd. Note that the pump-probe delay on the abscissa is bisected and the scale switches from linear to logarithmic. The transient valence band binding energies have been extracted by a fit to the data as indicated at the bottom of Fig. S1. Data for Gd are from Ref. 5. From the binding energy of the 5d minority and majority spin valence bands we calculated the transient exchange splitting. In parallel to the measurement of the exchange splitting, the dynamics of the MLD signal was determined from the $^8S_{7/2}$ high spin component at a photon energy of 36.8 eV as described in the previous section. The solid lines are single exponential fits to the data. Time constants and error bars are specified in the figure.

D. Sample quality

Lanthanide metals are extremely reactive, which makes the investigation of pure single crystals challenging. Even under ultra-high vacuum condition with a base pressure of $4 \cdot 10^{-11}$ mbar, which we achieve in our setup during ARPES measurements, a clean sample is affected by adsorbates within a few hours. Clean bulk single crystals of Gd and Tb are almost impossible to prepare. Tungsten was found to be a good choice of substrate for molecular beam epitaxy, because it is easy to handle and has a high melting point. The pseudo-hexagonal W(110) surface matches to the (0001) surface of Gd and Tb quite well, in fact the lattice mismatch is found to relax within five monolayers. Another advantage is the high surface energy of W(110) which favors a layer-by-layer growth of the rare-earth metals and prevents the formation of intermetallic alloys. However, cleaning tungsten is a challenge. We got the best result by heating the sample up to 1800 K in an oxygen atmosphere of $5 \cdot 10^{-8}$ mbar followed by a short flash up to 2100 K under UHV condition to force the stronger bound tungsten-oxides to desorb. The duration of cleaning cycles depends on the purity of the sample. We used LEED and ARPES as highly surface sensitive techniques to test the sample quality. Figures S5a) to c) show the LEED pattern and corresponding ARPES spectrum of the W(110) surface at each step of a cleaning cycle.

Films of 10 nm thickness (35 monolayers) were found to be suitable to study the magnetic behavior of Gd and Tb. They are thin enough to have their easy axis in plane and grow layer-

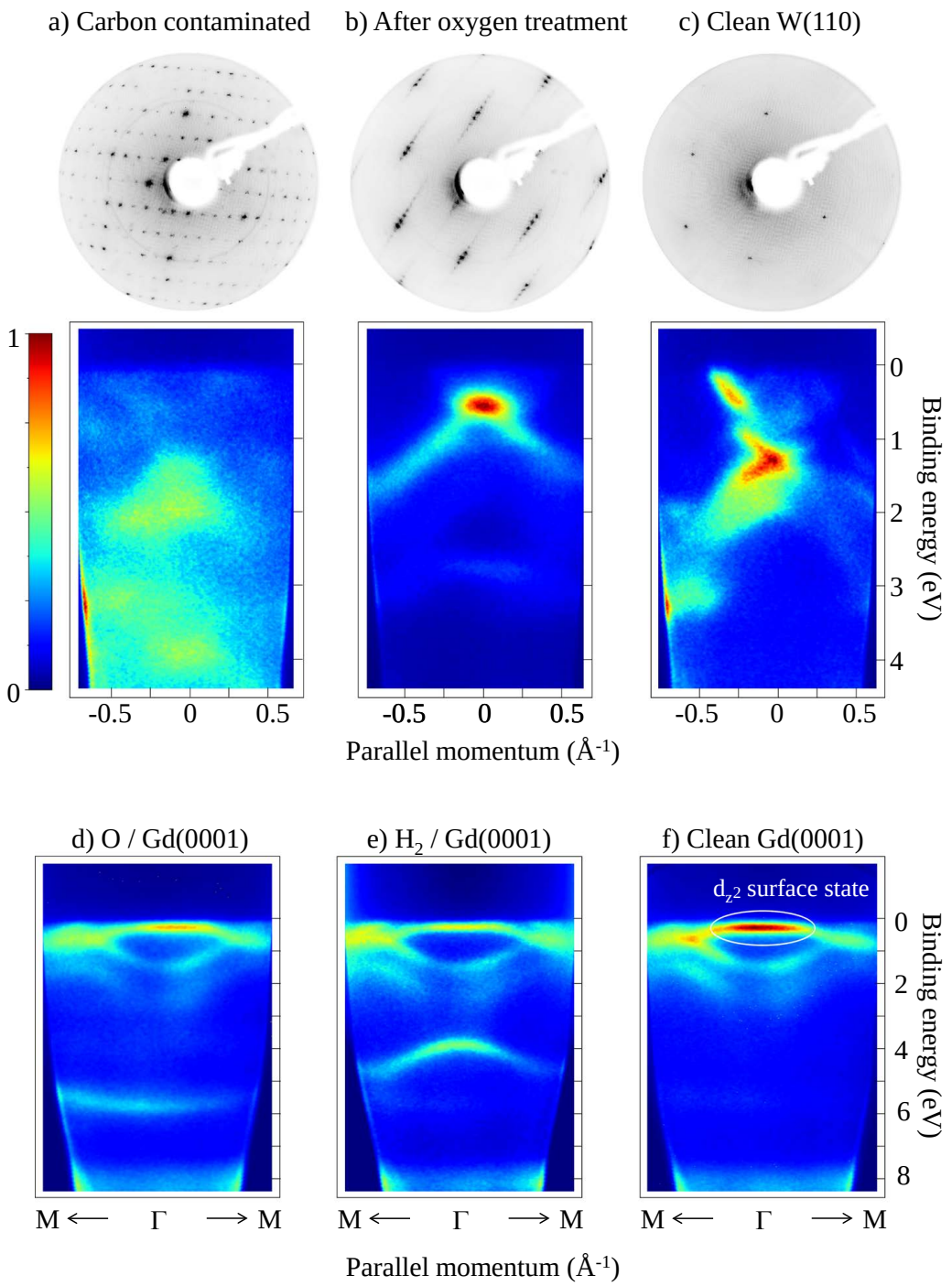

FIG. S5. Preparation of W(110) substrate and Gd(0001) film. LEED patterns and ARPES spectra in a false-color plot. LEED was recorded at 160 eV electron energy, static ARPES at 36.8 eV photon energy. a) Carbon contaminated, b) after oxygen treatment, c) clean W(110) surface after flash to 2100 K, d) Atomic oxygen and e) molecular hydrogen contamination on Gd(0001) f) Clean Gd(0001) surface. The surface-state intensity is highly sensitive to surface contaminations.

by-layer, yet are thick enough to show electronic bulk behavior. For the epitaxial growth of the lanthanides we use self-made evaporators, consisting of a tungsten crucible which is filled with 99.99% pure Gd or Tb. The crucible is heated by electron bombardment from surrounding tantalum filaments. Since the evaporation rate has an influence on the quality of the films we choose a well established rate of about 0.5 nm/min, monitored by a quartz microbalance. After degasing the evaporator we achieve a pressure of below $2 \cdot 10^{-10}$ mbar during evaporation. The best annealing temperature for our 10 nm films were 680 K for Gd and 880 K for Tb. The quality of the preparation is most easily monitored by the intensity of the d_{z^2} surface state in ARPES. Defects and adsorbates interfere with the surface state reducing its intensity. Figures S5 d) to f) show the typical spectra for atomic oxygen and molecular hydrogen adsorbates, as well as for the clean Gd(0001) surface. A small uptake of oxygen is unavoidable during the measurement as seen in Fig. S1. However, laser-induced desorption by the infrared pump pulse keeps contamination at an acceptable very low and stable level. A new sample was prepared every 6-8 hours. The low degree of oxygen contamination can be seen when comparing the measurement series in Fig. S1 with coverage-dependent O/Gd(0001) ARPES spectra [35].

II. SPIN-DYNAMICS SIMULATIONS

A. Extended two-temperature model

Figure S6 shows the temperatures of electron and phonon subsystems, T_{el} and T_{ph} upon laser excitation $P(t)$. They are computed with an extended two-temperature model (2TM) [26],

$$\begin{aligned} C_{\mathrm{el}}\frac{\partial T_{\mathrm{el}}}{\partial t} &= G_{\mathrm{el,ph}}(T_{\mathrm{ph}}-T_{\mathrm{el}}) + \frac{\partial}{\partial z}\kappa_{\mathrm{el}}\frac{\partial T_{\mathrm{el}}}{\partial z} - \dot{Q}_{\mathrm{5d}}\{\vec{S}_i^{\nu}\} + P(t) \\ C_{\mathrm{ph}}\frac{\partial T_{\mathrm{ph}}}{\partial t} &= G_{\mathrm{el,ph}}(T_{\mathrm{el}}-T_{\mathrm{ph}}) + \frac{\partial}{\partial z}\kappa_{\mathrm{ph}}\frac{\partial T_{\mathrm{ph}}}{\partial z} - \dot{Q}_{\mathrm{4f}}\{\vec{S}_i^{\nu}\} \end{aligned} \tag{S2.1}$$

where we take into account the exchange of thermal energy with the spin subsystems in a self-consistent way via [37]

$$\dot{Q}_{\nu} = -\frac{1}{V}\sum_i \frac{\partial \mathcal{H}}{\partial \vec{S}_i^{\nu}} \cdot \left[\frac{\gamma_{\nu}}{\mu_{\nu}}\vec{S}_i^{\nu}\times\vec{\zeta}_i^{\nu} - \alpha_{\nu}\vec{S}_i^{\nu}\times\frac{\partial \vec{S}_i^{\nu}}{\partial t}\right]. \tag{S2.2}$$

The parameters entering Eq. (S2.1) are the specific heat C_{λ}, the electron-phonon coupling $G_{\mathrm{el,ph}}$, the thermal conductivity κ_{λ} and the sample volume V. The 2TM parameters are taken from the Supplementary Methods of Ref. 5 assuming little differences between Tb and Gd. In the first term, the electron-phonon coupling $G_{\mathrm{el,ph}}$ quantifies the energy flow of the hot electron system to the colder phonon system. The second term describes the heat transport from the metal film into the substrate. The thermal conductivity of the tungsten substrate is enhanced by the phonon-contribution which becomes relevant at lower temperatures. It is necessary to include this contribution, because of the lower Curie temperature of Tb in comparison with Gd. For the calculations, we used the temperature-dependent phonon-thermal conductivity provided by Ref. 38.

The incorporation of the third term, as detailed in Eq. (S2.2), into our temperature model Eq. (S2.1) has mainly two effects. First, it takes into account the magnetic contribution to the energy flow, similar to the model in Ref. 5. This contribution is quantified by the second term in Eq. (S2.2) that is proportional to the damping constant α_{ν} (the first term giving the influence of stochastic thermal fluctuations). The corresponding specific heat in the orbital-resolved spin model hereby consists of (i) the contribution from the conventional atomistic spin Hamiltonian, *i.e.* the *inter*-atomic Heisenberg exchange, the magnetocrystalline anisotropy, and the Zeeman energy, as well as (ii) an additional contribution from the

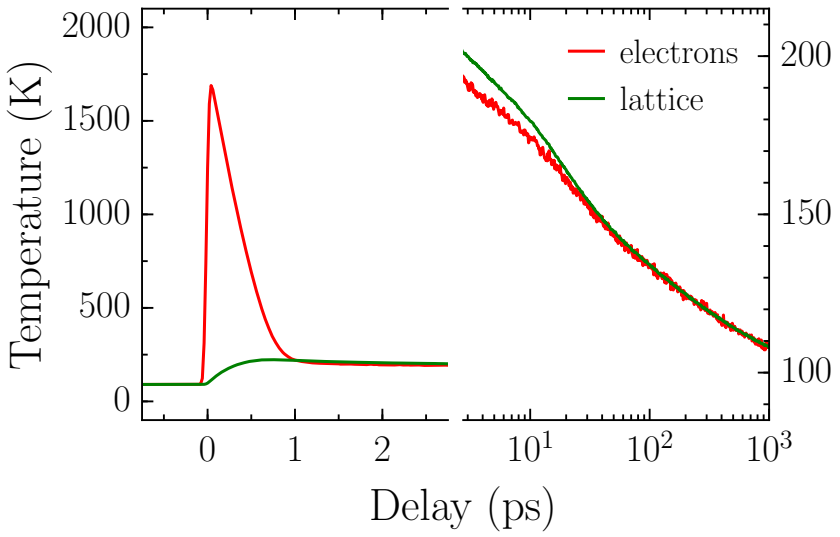

FIG. S6. Time evolution of the electron and phonon temperatures T_{el} and T_{ph} of the laser excited Tb film on tungsten, calculated with the extended two-temperature model.

intra-atomic exchange which is $C_{\mathrm{intra}} \propto -J_{\mathrm{intra}} \frac{d}{dT} \mathcal{L}(J_{\mathrm{intra}}/k_{\mathrm{B}}T)$, with $\mathcal{L}$ being the Langevin function. Second, Eqs. (S2.1)+(S2.2) provide an additional coupling between the electron and phonon temperatures beyond the direct electron-phonon coupling term $G_{\mathrm{el,ph}}$. Whereas in Gd this contribution was negligible due to the weak spin-phonon coupling $\alpha_{\mathrm{4f}}^{\mathrm{Gd}} \sim 0.001$, it has to be considered in the case of Tb where $\alpha_{\mathrm{4f}}^{\mathrm{Tb}} \sim 0.1$.

In the practical implementation of this temperature model it must be taken into account that integrating Eq. (S2.2) is not energy conserving. To keep the energy constant, we compute the numerically exact energy in the spin system by evaluating the spin Hamiltonian Eq. (1) every $\sim 10^2$ fs and use this value as a corrector. This is in particular necessary at quasi-equilibrium where fluctuations [left term in Eq. (S2.2)] and dissipations [right term in Eq. (S2.2)] cancel almost completely.

B. Ultrafast orbital-resolved demagnetization dynamics

For the theoretical description of the ultrafast demagnetization in the rare-earth metals, we use the orbital-resolved spin model introduced in the main text. As depicted in Fig. 1 of the main text we distinguish between the localized 4f-moments with $\mu_{\mathrm{4f}}^{\mathrm{Tb}} = 9\,\mu_{\mathrm{B}}$ and the itinerant 5d-moments with $\mu_{\mathrm{5d}}^{\mathrm{Tb}} = 0.34\,\mu_{\mathrm{B}}$ [36]. Since the optical laser pump-pulse only

excites the valence electrons, we couple the electron heat bath with transient temperature T_{el} exclusively to the 5d spins of the valence electrons. The 4f spin system interacts with the phonon heat bath with transient temperature T_{ph}.

We solve the orbital-resolved spin Hamiltonian $\mathcal{H}$ (Eq. (1), main text) to derive the local field contributions $-\partial\mathcal{H}/\partial\vec{S}_i^{\nu}$. The *inter*-atomic Heisenberg exchange interactions J_{ij} entering Eq. (1) are taken from Fig. S10a, the *ab initio* calculated *intra*-atomic exchange interaction is $J_{\mathrm{intra}}^{\mathrm{Tb}} = 212\,\mathrm{meV}$. Employing the first-principles-derived exchange constants, we simulate a spin system with 165 888 Tb atoms (331 776 spins) taking into account exchange interactions up to the 20^{th} nearest neighbor. For the Tb magnetocrystalline anisotropy we take into account an uniaxial anisotropy energy of $d_{2,\mathrm{Tb}} = -16.5\,\mathrm{meV}$ (easy plane) and a basal-plane anisotropy of $d_{6,\mathrm{Tb}}^{6} = 48\,\mu\mathrm{eV}$ (easy b-axis) [27], which for simplicity are expressed in terms of the spherical coordinates ϑ_i and φ_i of the 4f-spins. Note that for Gd the calculated intra-atomic exchange is slightly lower $J_{\mathrm{intra}}^{\mathrm{Gd}} = 137\,\mathrm{meV}$ and the magnetization has an easy c-axis with $d_{2,\mathrm{Gd}} = 27\,\mu\mathrm{eV}$ [28], hence we can neglect $d_{6,\mathrm{Gd}}^{6}$.

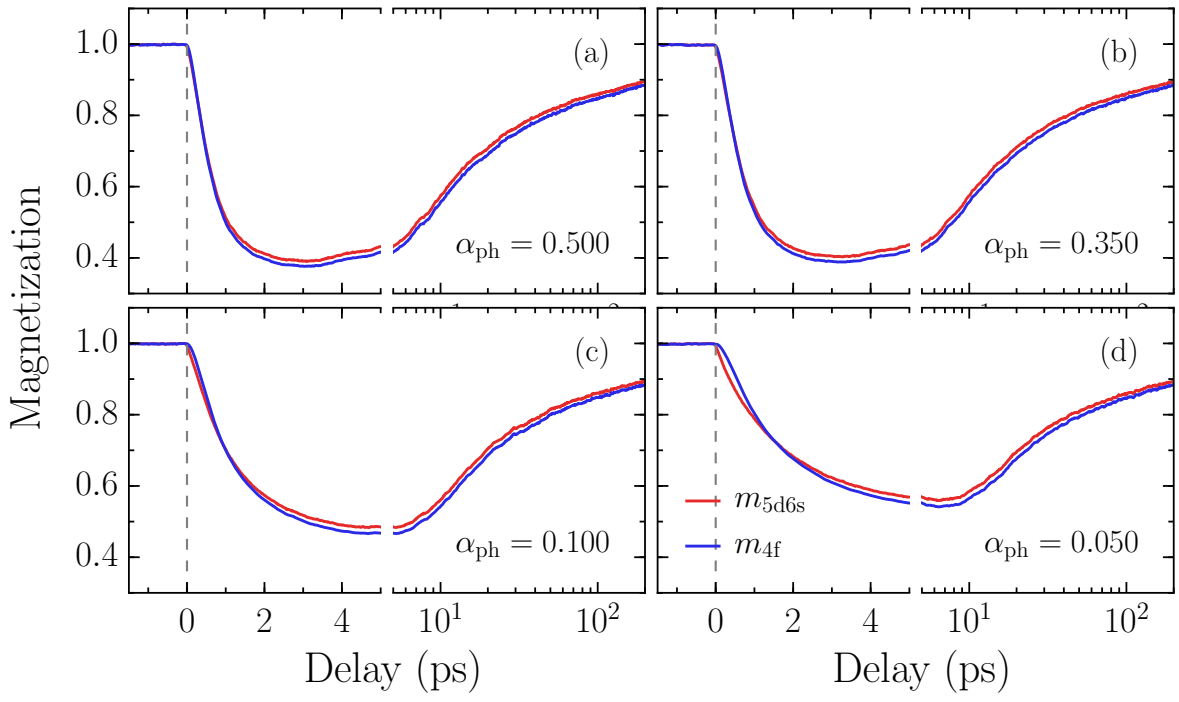

FIG. S7. Orbital-resolved demagnetization of Tb upon NIR-laser excitation calculated for different values of the spin-phonon coupling $\alpha_{4\mathrm{f}}$ with $\alpha_{5\mathrm{d}} = 0.00013$ kept constant.

To compute the effective field that enters the stochastic Landau-Lifshitz-Gilbert equation thermal fluctuations are included in the form of Gaussian white noise with

$$\langle \vec{\zeta}_i^{\nu} \rangle = 0 \quad \text{and} \quad \langle \vec{\zeta}_i^{\nu}(0) \vec{\zeta}_j^{\kappa}(t)^{\dagger} \rangle = \frac{2\alpha_i^{\nu} \mu_i k_{\mathrm{B}} T_{\nu}}{\gamma_i} \delta_{ij} \delta_{\nu\kappa} \delta(t) \tag{S2.3}$$

where the temperature T_ν of the thermal reservoir is the electron temperature for the 5d spins and the phonon temperature for the 4f spins (see Fig. 1, main text). The computation of the exchange constants is described in detail below.

Figure S7 shows the demagnetization and remagnetization dynamics of Tb, calculated from the orbital-resolved spin model for different values of the spin-phonon coupling $\alpha_{4\mathrm{f}}$. For $\alpha_{4\mathrm{f}}$ larger than about 0.35 the demagnetization time scale becomes limited by the electron phonon equilibration time scale, hence the demagnetization dynamics does not change significantly anymore when $\alpha_{4\mathrm{f}}$ is increased further. For smaller values of $\alpha_{4\mathrm{f}}$ we see a slowing down of the demagnetization dynamics which also affects the 5d electron dynamics due to the strong intra-atomic exchange coupling.

C. Tb density of states

The *intra*-atomic exchange and 5d exchange splitting have been calculated employing the LSDA+U approach [41] for correlated electrons with the inclusion of 4f states in the valence band in order to compute accurately the interaction between 4f and 5d states. This calculation is based on the full-potential linear augmented plane wave (FP-LAPW) method, as implemented in the band structure program ELK (http://elk.sourceforge.net/). Spin-orbit coupling has been included in the calculation. The full Brillouin zone has been sampled by about 5000 k-points. We have employed $U = 0.15$ Hartree for the 4f states, and the double counting has been treated in the fully localized limit. The obtained 4f peak positions are in a reasonable agreement with the experimentally observed ones. The calculated partial density of states (DOS) is shown in Fig. S8. One spin-minority 4f level appears at 3 eV binding energy, in agreement with our photoemission measurements shown in Fig. 2 of the main text. The spin-split 5d bands are located in a several eV wide energy range around the Fermi energy.

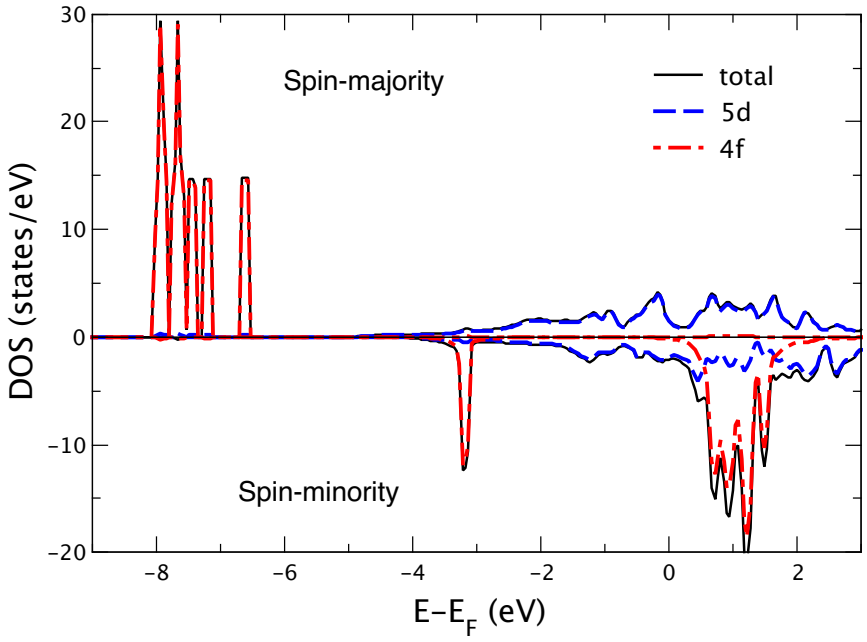

FIG. S8. *Ab initio* calculated partial and total density of states of Tb. One occupied 4f spin-minority orbital is located at 3 eV binding energy, spin-majority occupied 4f states are located at 7-8 eV binding energy, and the manifold of unoccupied 4f states is located above the Fermi energy E_{F}. The spin-polarized 5d states form a several eV wide band near the Fermi energy.

D. 5d exchange-splitting

On the one hand, the 5d magnetic moment does not behave as an ideal Heisenberg moment. Its magnitude depends strongly on its environment, mainly the surrounding 4f moments. On the other hand, the 5d moment does not fully originate from the 4f magnetization as would be expected in the Stoner picture, since it also survives above the critical temperature. In the complex non-equilibrium situation with the 4f magnetization at an elevated temperature, and the 5d spin subsystem at a different temperature, leading to their non-collinear alignment, we evaluate the resulting exchange splitting by *ab initio* methods. Notably, the exchange splitting depends on the magnetic disorder of the 4f moments. When 4f and 5d systems are not in equilibrium, the exchange splitting also depends on the the average relative angle θ between $\boldsymbol{S}^{5\mathrm{d}}$ and $\boldsymbol{S}^{4\mathrm{f}}$, and here we evaluate this dependence.

We employ the same *ab initio* description as for the calculation of the intra-atomic exchange based on the linear plane wave method (see Sec. II C), while the directions of the spd

magnetic moments are constrained [5] so that their angle w.r.t. the 4f momentum direction is θ. For this constrained system we calculate the resulting band structure and extract the exchange splitting of the valence bands at the Γ point. The dependence on θ appears to be approximately quadratic, as shown in Fig. S9.

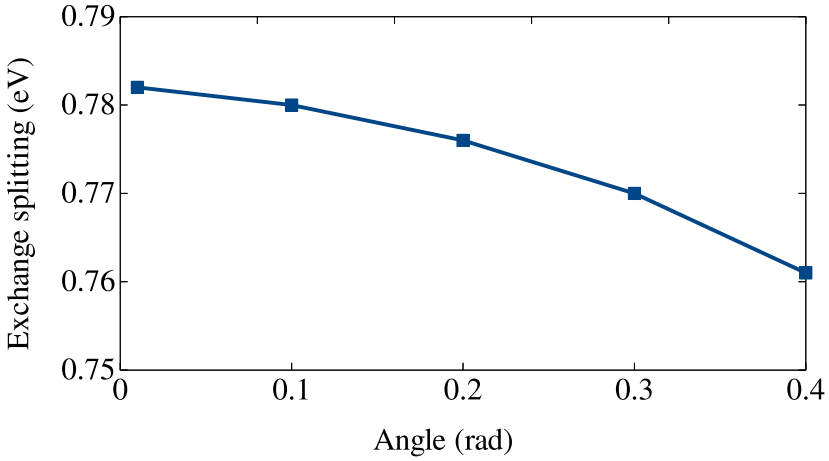

FIG. S9. *Ab initio* computed d-band exchange splitting at the Γ point as a function of the angle θ between the non-collinear 5d and 4f spin moments of Tb.

E. Tb exchange constants and equilibrium magnetization

The calculations of the *inter*- and *intra*-atomic exchange constants require different capabilities of computational methods. Therefore we employed two completely different theoretical approaches. The present *ab initio* calculations of the *inter*-atomic exchange constants in Tb are based on the tight-binding linear muffin-tin orbital (TB-LMTO) method [39] employing the atomic-sphere approximation (ASA). The Vosko-Wilk-Nursair exchange potential has been used within the local spin-density approximation [40]. The 4f electrons were included as core electrons in this calculation, an approach which we found to overcome some limitations of the local spin-density approximation (LSDA) method and improve its accuracy. This method has already been used to successfully evaluate the magnetic properties and magnetostriction of Gd and several rare-earth-based compounds. For the calculation of Tb we used the experimental lattice parameters $a = 3.59$ Å and $c = 5.714$Å.

The magnetic interactions were mapped onto an effective Heisenberg Hamiltonian (Eq. (1)

in the main text). Exchange interactions between different sites, J_{ij}, were calculated employing the magnetic force theorem [42], which allows us to obtain the exchange constants from a self-consistently calculated collinear ground state, described by spin-dependent Green functions G^{σ} ($\sigma = \uparrow, \downarrow$ is the spin index) and the magnetic field resulting from the exchange-correlation potential, $B_{xc}(\mathbf{r}) = V^{\uparrow}(\mathbf{r}) - V^{\downarrow}(\mathbf{r})$. The Liechtenstein formula [40] then provides pair-wise exchange interactions J_{ij} as

$$J_{ij} = \frac{1}{\pi}\mathrm{Im}\int_{-\infty}^{E_{\mathrm{F}}} \mathrm{d}E \int_{\Omega_i} \mathrm{d}\mathbf{r} \int_{\Omega_j} \mathrm{d}\mathbf{r}' B_{xc}(\mathbf{r})\, G^{\uparrow}\left(\mathbf{r}, \mathbf{r}', E^{+}\right) B_{xc}(\mathbf{r}')\, \bar{G}^{\downarrow}\left(\mathbf{r}', \mathbf{r}, E^{-}\right), \qquad \text{(S2.4)}$$

where Ω_i denotes the sphere with center at the i-th atom position, E_{F} is the Fermi level, and $E^{\pm} = \lim_{\alpha \to 0} E \pm \mathrm{i}\alpha$. The calculated exchange constants for Tb are shown in Fig. S10a as a function of distance.

Figure S10b shows the equilibrium magnetization as a function of temperature, calculated with atomistic spin-dynamics simulations (see below) using the exchange integrals J_{ij} depicted in Fig. S10a up to a cutoff distance of $r_{ij} \leq 11$ Å $\approx 3.1\ a$. The 5d magnetization closely follows the 4f magnetization without significant decoupling between the two moments. We obtain a theoretical Curie temperature of 214 K, which is in excellent agreement with Ref. 36 and implies that our orbital-resolved spin model with *ab initio* exchange constants describes the localized and itinerant ferromagnetism of Tb adequately.

The spin-spiral phase that is found in the narrow temperature range between $T_{\mathrm{C}} = 220$ K and $T_{\mathrm{N}} = 230$ K is not present in our model either due to the lack of Dzyaloshinskii-Moriya interactions (DMI) in the spin Hamiltonian or the lack of weak exchange frustration of the isotropic Heisenberg interaction (see Fig. S10a). However, since the experiments were performed in the ferromagnetic phase, we do not expect any noticeable effect from neglecting the DMI.

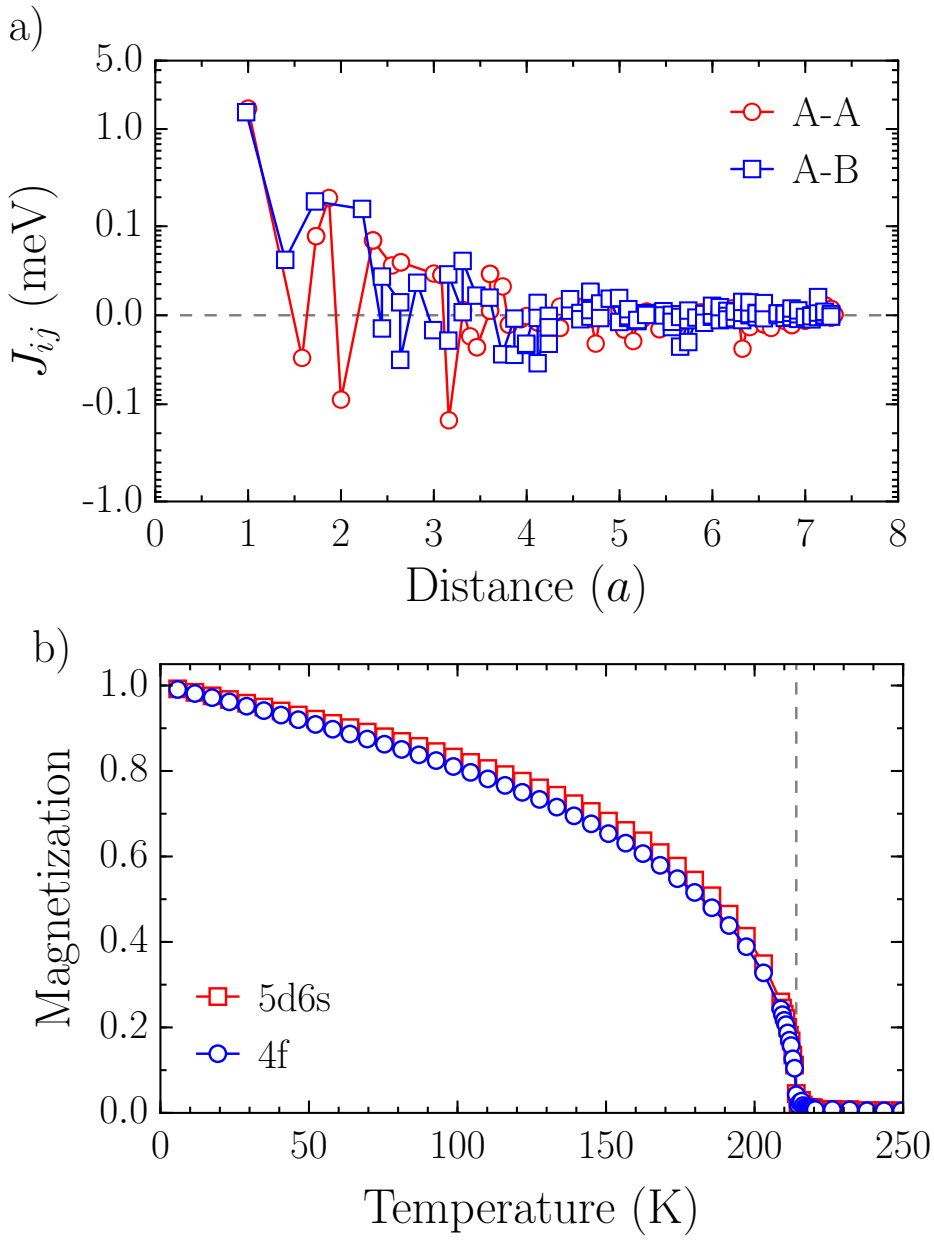

FIG. S10. *Ab initio* calculated *inter*-atomic exchange constants J_{ij} and resulting equilibrium magnetization M(T) of Tb. a) Heisenberg exchange J_{AA} and J_{AB}, for atoms A and B in the different (0001)-layers of the hexagonal closed-packed (hcp) crystal structure. Note the hyperbolic scaling of the vertical axis. b) The equilibrium magnetization of Tb for the itinerant 5d spins, which mediate the *inter*-atomic Heisenberg exchange coupling J_{ij}, and for the localized 4f spins shows comparable temperature-dependence due to the strong *intra*-atomic exchange coupling. The calculated Curie temperature of 214 K is in excellent agreement with the experimentally determined Curie temperature [36].